

Article

Probing the Impact Energy Release Behavior of Al/Ni-Based Reactive Metals with Experimental and Numerical Methods

Kerong Ren ^{1,2}, Rong Chen ^{1,*}, Yuliang Lin ^{1,*}, Shun Li ³, Xianfeng Zhang ² and Jun Dong ²

¹ College of Liberal Art and Sciences, National University of Defense Technology, Changsha 410073, China; ren_kerong@163.com

² Aviation Maintenance NCO Academy, Air Force Engineering University, Xinyang 464000, China; zhangxianfeng013@163.com (X.Z.); 15716405390@139.com (J.D.)

³ College of Aeronautics and Astronautics, National University of Defense Technology, Changsha 410073, China; linudt@163.com

* Correspondence: r_chen@nudt.edu.cn (R.C.); ansen_liang@163.com (Y.L.); Tel.: +86-0731-8700-1881 (R.C.); +86-0731-8700-1853 (Y.L.)

Received: 7 March 2019; Accepted: 26 April 2019; Published: 28 April 2019



Abstract: Reactive metals (RMs) are a new class of material that can withstand mechanical loads and chemically react to release large amounts of heat under strong impact loading. They are gradually becoming widely used in defense and military fields, including for high-efficiency warheads and reactive armor. For the numerical simulation method considering the combined mechanical-thermo-chemical process for the impact energy release behavior of the RMs, the Al/Ni-based RMs were investigated in this work by combining experiments, theoretical calculations and a numerical simulation. Three kinds of Al/Ni-based RMs (Al-Ni, Al-Ni-CuO and Al-Ni-MoO₃), were prepared using the hot-pressing forming process. Firstly, the compressive behavior and the parameters of the Johnson-Cook constitutive model were obtained using a mechanical testing machine and split Hopkinson pressure bars (SHPB). Secondly, the parameters of the equation of state (EOS) under the medium and low pressure conditions of the Al/Ni-based RMs, which were seen as porous mixtures with high theoretical material density percentages (TMD%), were calculated based on the cold-energy superposition theory and the Wu-Jing method. Third, the impact energy release behaviors of the three RMs were studied with direct ballistic tests. The shock temperatures at different impact velocities were calculated based on the existing shock-induced chemical reaction thermo-chemical model while considering the chemical reaction efficiency, the relationship between the shock temperature and the extent of the chemical reaction was established, and the parameters of the relevant chemical kinetic equations were fitted. Finally, the user's subroutines defining the material model were implemented to update the stresses in the solids elements in LS-DYNA. The model was based on the Johnson-Cook constitutive model with consideration of the mechanical-thermo-chemical coupling effect, which was verified by the experimental results. The results show that the constitutive model developed in this work can describe the impact energy release behavior of the Al/Ni-based RMs.

Keywords: Al/Ni-based reactive metals (RMs); mechanical properties; impact energy release behavior; numerical simulation considering the mechanical-thermo-chemical coupling effect

1. Introduction

Over the past few decades, energetic fragments have been proposed in the development of efficient damage warhead technology. This term refers to a new-type warhead damage element that is combined with characteristics of penetration similar to those of blunt fragment and shock-induced

energy release. Compared with a traditional blunt fragment, an energetic fragment can greatly improve the damage effect of a warhead. The materials used to prepare for the energetic fragment are called reactive metals (RMs) [1,2], and they usually contain metal elements such as Al, Ni, Ti, W, Zr and Si and small amount of metal oxides such as Fe_2O_3 , CuO, MgO, and MoO_3 . To improve the power of the warhead and expand the application fields of the RMs, many studies have mainly focused on mechanical properties [3–12] and impact energy release behavior [13–22]. Dynamic mechanical properties are important for the RMs. At medium and low strain rates, classical experiments such as the Taylor test [3,10–12] and Hopkinson bars [4,8], have been widely used to study the dynamic mechanical behavior of RMs. At high strain rates, using the technology of an explosive loading device or a compressive gas gun, a parallel-plate impact experiment [5–8] is a common experimental method used to measure the Hugoniot data of materials.

The direct ballistic experiment that was proposed by Ames [13,14] can measure the chemical release energy of the RMs under different impacts. This experiment can also calculate the relationship between the physical quantities (such as the pressure, specific volume, and temperature, etc.) and the chemical reactivity under impact. When this information is combined with the shock-induced release theory, the characteristic parameters of a shock-release chemical reaction can be obtained. The experimental device consists of a machine gun and a sealed cylindrical test chamber, with one end being a thin metal plate (i.e., a target skin) and with a hard impact anvil fixed inside the chamber. After the bullet made of the RMs penetrates the thin plate at a certain velocity, the temperature in the test chamber rises due to the chemical reaction, leading to an increasing pressure. The energy release behavior can be investigated as follows: First, measuring the pressure time-history curve in the test chamber; second, filtering the high-frequency signal with a low-pass filter to obtain the quasi-static pressure in the test chamber; and finally, calculating the energy and efficiency produced by the reaction of the RMs.

The theoretical studies for impact energy release behavior can be divided into three categories by Thadhani [6,7] according to the action of the impact wave on the materials, i.e., shock modification (SM), shock-assisted chemical reaction (SACR) and shock-induced chemical reaction (SICR). Zhang [23,24] established a thermochemical model of SICR that considered the chemical reaction extent according to the impact kinetics and the chemical reaction kinetics method. The relationships among the shock temperature, impact pressure, and reaction release energy were obtained with this model.

In addition, with consideration of the unique microstructure of the RMs, a micro-finite element numerical simulation is a common means used to obtain the mechanical response under impact. Scholars [25–32] have researched many micro-model construction methods of the RMs prepared by different techniques. These methods can accurately calculate the equation of state (EOS) of the material from the microscopic perspective. Austin [30] established various micro-finite element models of the Al/Ni-based RMs according to the scanning electron microscope (SEM) images, and calculated the space-time distribution of the physical parameters such as temperature under an impact based on the Euler method. However, a microscopic simulation considering the mechanical-thermo-chemical coupling effect can limit the size of the specimens and it cannot be directly used for engineering applications. Therefore, further research on macroscopic simulation is urgently needed.

In the present work, based on a combination of experiment and simulation, the mechanical properties and the impact energy behavior of Al-Ni based RMs were studied. First, the mechanical behavior of the materials was studied using a mechanical testing machine and a SHPB test apparatus, and the Johnson-Cook constitutive model parameters of the material were obtained. Then, the Hugoniot parameters of the materials were calculated using the cold energy superposition method and the Wu-Jing method. Second, the parameters of the chemical reaction kinetic equation of the materials were fitted adopting direct ballistic experiments and a shock-induced chemical reaction model. Finally, the mechanical-thermo-chemical coupled user-defined constitutive model was developed in LS-DYNA software and the macroscopic numerical simulation of the impact energy behavior of the materials was carried out based on the model.

2. Materials and Specimens

2.1. Specimen Preparation

Three kinds of Al/Ni-based RMs, i.e., Al-Ni, Al-Ni-CuO, and Al-Ni-MoO₃ (referred to as AN, ANC, and ANM, respectively), were prepared using the hot-pressing forming technology, with the Al powder, Ni powder, CuO powder and MoO₃ powder used as raw materials. The descriptions of these powders are as follows:

- Al powder (Figure 1a), spherical particles, average particle diameter: 3~4 μm;
- Ni powder (Figure 1b), spherical particles, average particle diameter: 10 μm;
- CuO powder (Figure 1c), spherical particles, average particle diameter: 10 μm;
- MoO₃ powder (Figure 1d), flake particles, average particle size: 1~2 μm.

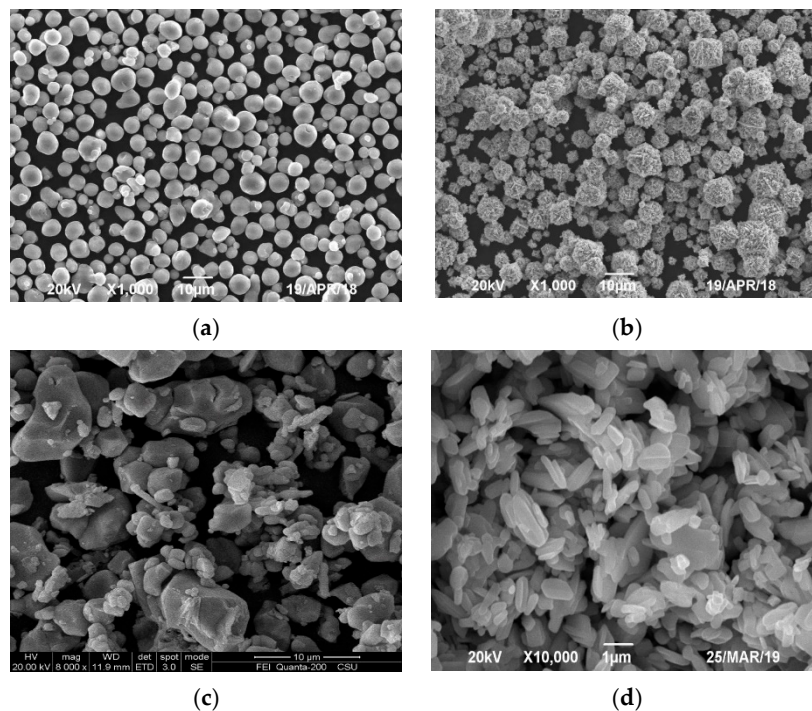


Figure 1. The scanning electron microscope (SEM) images of the raw materials: (a) Al powder; (b) Ni powder; (c) CuO powder; (d) MoO₃ powder.

The molar ratio of Al and Ni was 2:1 for the three materials, and the mass fractions (MF) of the CuO powder and the MoO₃ powder were less than 5% for the ANC and the ANM. The preparation steps were as follows: (1) fill the powders in the mold after they were sufficiently mixed by the ball mill; (2) raise the temperature to 400 °C with a heating rate of 10 °C/min, and isothermally burning the powders for 1 h with a pressure of 380 MPa; (3) cool the specimens to room temperature in the furnace. The components of each material and the theoretical material densities (TMD), actual material densities (AMD) and TMD percentages (TMD%) of all of the fabricated specimens are listed in Table 1.

Table 1. Components, densities, and TMD% of specimens.

Materials	Component	AMD ¹ (g/cm ³)	TMD ² (g/cm ³)	TMD% ³
AN	Al and Ni molar ratio 2:1	4.098	4.224	97.02%
ANC	Al and Ni molar ratio 2:1, MF(CuO) < 5%	4.141	4.282	96.70%
ANM	Al and Ni molar ratio 2:1, MF(MoO ₃) < 5%	4.076	4.241	96.12%

¹ AMD values are measured by the densitometer. ² TMD values are calculated based on the actual size of the specimens. ³ TMD% are equal to the ratio of AMD to TMD, i.e., TMD% = (AMD/TMD) × 100%.

2.2. Microstructures

Specimens with diameters of 20 mm were prepared in the epoxy mount using dibutyl phthalate as a solvent and ethylenediamine as the curing agent. The specimens were polished by sandpapers of up to #4000, then polished with the diamond paste. The microstructures were observed with a S4800 field emission scanning electron microscope (HITACHI Ltd., Tokyo, Japan).

Figure 2 shows the microstructures of untested AN, ANC, and ANM. It can be seen that all of the microstructures have the piebald characteristics, i.e., the Ni phase (the smaller area and lighter color) is surrounded by the Al phase (the larger area and darker color). Some hole defects exist between the Al phase and the Ni phase. These defects were formed in the hot-pressing forming process. The medium gray phases attached to the Ni phase are CuO and MoO₃. According to the analysis above, the three Al/Ni-based RMs can be approximated as a porous material with high TMD%.

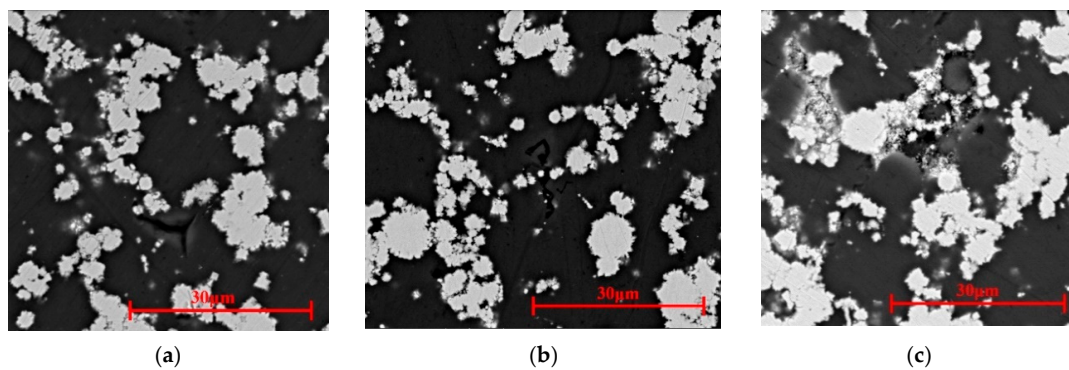


Figure 2. Microstructures of Al/Ni-based RMs: (a) AN; (b) ANC; (c) ANM.

In addition, the hot-pressing forming process was carried out in an oxygen-free environment. The XRD tests were performed on the finished samples by Smartlab X-ray diffractometer (RIGAKU Corp., Tokyo, Japan) (the working voltage and the current were 40 KV and 40 mA, respectively, the X-ray source was CuK α ($\lambda = 0.1542$ nm), and scanning range was a 2θ angle from 20° to 90° , with a scanning speed of 30/min). The test results are shown in Figure 3.

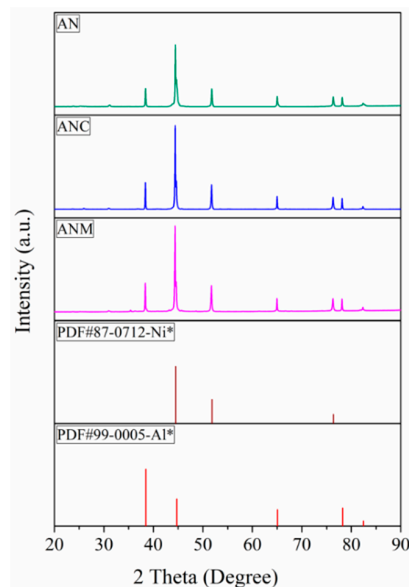


Figure 3. XRD test results of Al/Ni-based reactive metals. (* Standard X-ray diffraction powder patterns, National Bureau of Standards (U.S.), Circular 359 (1953) 1-1, measured by Howard E. Swanson and Eleanor Tatge).

It can be seen from the test results that the three Al/Ni-based reactive metals components are mainly composed of Al and Ni elements, and no other Al/Ni intermetallic compounds or Al/Ni oxides were observed. Additionally, because the mass fractions of CuO and MoO₃ in the ANC and ANM are extremely low, their diffraction intensity might have been low. Thus, the metal oxides added in the ANC and ANM are not clearly observed in these XRD tests.

3. Mechanical Properties

3.1. Quasi-Static Compressive Mechanical Properties

The cylindrical specimens with sizes of $\Phi 10 \text{ mm} \times 10 \text{ mm}$ were taken from the hot-press forming block using the electric discharge wire cutting, and the round surfaces of their ends were polished with sandpaper to remove the attached metal oxides. The static compressive test was carried out on the WDW-100 electronic universal mechanical testing machine (INSTRON Corp., Boston, MA, USA) at room temperature, with an initial loading strain rate of $1.0 \times 10^{-2} \text{ s}^{-1}$. Three specimens were tested for each type of the Al/Ni-based RMs to obtain the room temperature quasi-static compressive performance curves.

Figure 4 shows the quasi-static compressive stress-strain curves. It can be seen that the yield stresses of AN, ANC, and ANM are $202 \pm 10 \text{ MPa}$, $200 \pm 3 \text{ MPa}$ and $190 \pm 2 \text{ MPa}$, respectively, and the yield strains are all $\sim 5\%$ (where the starting point of the plateau after the nonlinear elastic segment was considered to be the yield point). None of the specimens were damaged even though the true strain exceeded 50%.

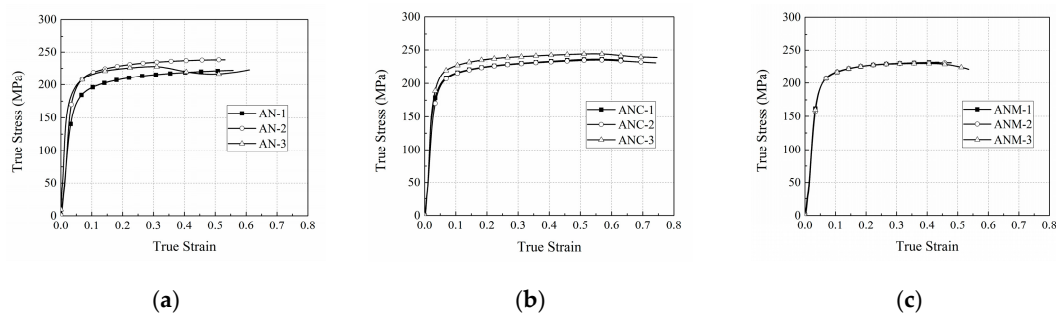


Figure 4. Quasi-static compressive stress-strain curves of three Al/Ni-based RMs: (a) AN; (b) ANC; (c) ANM.

Moreover, due to the end constraint caused by the nonuniform distribution of the frictional force on all parts of the surface of the specimens during continuous compression, there is a local damage phenomenon around the sample. Therefore, the mechanical behavior curve obtained after the local damage cannot reflect the true quasi-static stress-strain relationship of the materials, so the compression stroke of the material testing machine is controlled to be approximately 4–5 mm to ensure that the sample do not exhibit local damage during compression. The lateral deformation of the inner layer of the specimens is hindered by the outer layer and the outer layer was under a lateral-radial complex loading that cause the local damage phenomenon, which shows the excellent ductility of these Al/Ni-based RMs.

3.2. Dynamic Compressive Mechanical Properties

The Split Hopkinson pressure bars test apparatus (shown in Figure 5) was used to measure the dynamic compressive mechanical properties of the materials. The device is mainly composed of the bullet, the incident bar, the transmitted bar and specimen ($\Phi 8 \text{ mm} \times 3 \text{ mm}$), etc. The experimental principle is mainly the measurement of the incident wave (ε_i) in the incident bar, of the reflected wave (ε_r) from the interface between the incident bar and the specimen, and of the transmitted wave (ε_t) in the transmitted bar using the strain gauge mounted on the incident bar and the transmitted bar. Then

the stress-strain (σ - ε) relationship is derived according to the one-dimensional stress wave theory as follows [33]:

$$\sigma = \frac{A \cdot E}{A_0} \varepsilon_t \quad (1)$$

$$\varepsilon = -\frac{2C_0}{l_0} \int_0^t \varepsilon_r d\tau \quad (2)$$

where A_0 and l_0 are the original length and the cross-sectional area of the specimens, respectively; A , E and C_0 are the cross-sectional area, elastic modulus and elastic wave velocity of the bars, respectively; and t is the time.

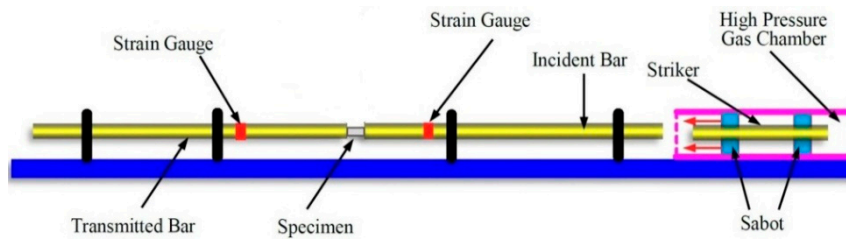


Figure 5. Schematic diagram of split Hopkinson pressure bars (SHPB).

A copper shaper was arranged at the front of the incident bar, producing constant strain rate loading under the three working conditions (2300 – 3000 s^{-1} , 4400 – 4900 s^{-1} and 5500 – 5900 s^{-1}). Figure 6 shows the true stress-strain curves of AN, ANC, and ANM at different loading strain rates. The yield point of the AN material under a strain rate of 2950 s^{-1} is shown as an example in Figure 4a (where the starting point of the plateau after the nonlinear elastic segment is considered to be the yield point). It can be seen that under the dynamic loading, the compressive mechanical behaviors of the three materials show obvious elastoplasticity. Their plastic strain values reached approximately 1.0 – 1.2 , so their plasticity was so good that can be approximated as power hardening. No damage occurred during loading, even when the strain rate was above 6000 s^{-1} , and the true strain was as high as 100 – 120% .

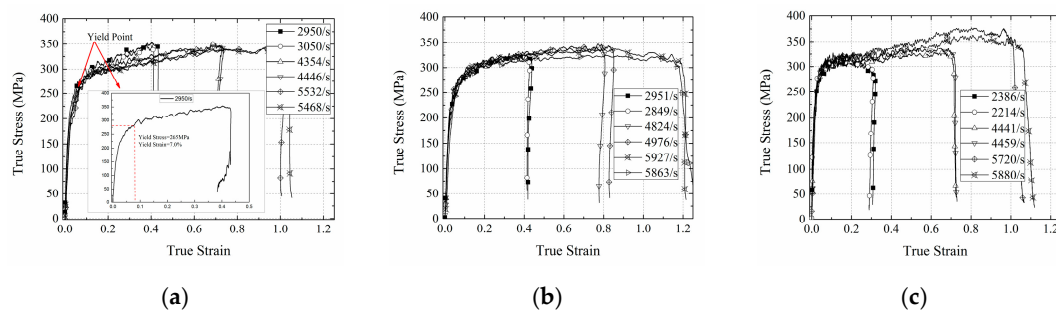


Figure 6. Results of the dynamic compressive experiments for the three Al/Ni-based RMs: (a) AN; (b) ANC; (c) ANM.

The yield stress and the yield strain of the three Al/Ni-based RMs under strain rates from $1.0 \times 10^{-2} \text{ s}^{-1}$ to about $6.0 \times 10^3 \text{ s}^{-1}$, and selected from the above results of the dynamic compressive experiment, are listed in Table 2.

Three conclusions can be obtained, as follows:

- (1) The yield points of the three Al/Ni-based RMs are all sensitive to the strain rate, and the yield stress and strain both increase with an increasing strain rate.
- (2) The yield strain greatly change with the strain rate increasing, and the degree from large to small is that of AN, ANC, and ANM. The yield stress experience little change with increase of the

strain rate, which was in the range of 200–300 MPa. When the strain rate is less than 3100 s^{-1} , the yield stresses from large to small are those of AN, ANC, and ANM; when the strain rate is above 3100 s^{-1} , the yield stresses from large to small are those of ANM, AN and ANM.

- (3) The different metal oxides added in the Al/Ni-based EMSs have different effects on the yield point. In the experimental strain rate range, the CuO addition cause the yield stress of the ANC to be lower than that of AN. In addition, at different strain rates, adding MoO_3 can lead to the yield strain of ANM significantly decreasing. When the strain rate is less than 3100 s^{-1} , the yield stress decreases. When the strain rate is greater than 3100 s^{-1} , the yield stress is significantly increased compared with that of AN.

Table 2. Yield points of three Al/Ni-based RMs under different strain rates.

Materials	Strain Rate (s^{-1})	Yield Stress (MPa)	Yield Strain (%)
AN	0.01	202 ± 10	5.9 ± 0.4
	3000 ± 50	277 ± 12	7.3 ± 0.3
	4400 ± 46	282 ± 9	9.2 ± 0.5
	5500 ± 32	290 ± 6	12.5 ± 0.4
ANC	0.01	200 ± 3	5.6 ± 0.1
	2900 ± 98	265 ± 10	6.4 ± 0.3
	4900 ± 76	275 ± 8	9.0 ± 0.5
	5900 ± 27	290 ± 9	13.1 ± 0.8
ANM	0.01	190 ± 2	4.8 ± 0.2
	2300 ± 86	265 ± 13	3.4 ± 0.5
	4400 ± 59	295 ± 10	5.5 ± 0.5
	5800 ± 80	305 ± 5	6.8 ± 0.5

3.3. Constitutive Model

The Johnson-Cook (J-C) constitutive model [34] is an empirical viscoplastic constitutive model. The flow stress σ_y is described as follows:

$$\sigma_y = \left(A + B \varepsilon_{\text{eff}}^p n' \right) \left(1 + C \ln \dot{\varepsilon}^* \right) \left[1 - (T^*)^m \right] \quad (3)$$

$$T^* = (T - T_r) / (T_m - T_r) \quad (4)$$

where A , B and C are the pending parameters, n' is the work hardening index, $\varepsilon_{\text{eff}}^p$ is the equivalent plastic strain, $\dot{\varepsilon}^* = \dot{\varepsilon} / \dot{\varepsilon}_0$ ($\dot{\varepsilon}_0$ is the reference strain rate, which is $1 \times 10^{-2} \text{ s}^{-1}$), T is the current temperature of the specimen, T_r is the room temperature (298 K), and T_m is the melting point of the materials. Under a high strain rate, the heat converted from the plastic work causes the specimen temperature to gradually increase during the deformation process. The temperature in the temperature softening term of the Johnson-Cook model is not the initial temperature of the experiment. The calculation is complicated because the temperature item may be updated at any time. To simplify the simulation process, the Johnson-Cook model was modified [35], and the adiabatic temperature rise (ΔT) after the plastic deformation was used instead of $(T - T_r)$, which is shown as follows [36]:

$$\sigma_y = \left(A + B \varepsilon_{\text{eff}}^p n' \right) \left(1 + C \ln \dot{\varepsilon}^* \right) \left[1 - (\Delta T / (T_m - T_r))^m \right] \quad (5)$$

$$\Delta T = \frac{\beta}{\rho C_p} \int_0^\varepsilon \sigma d\varepsilon \quad (6)$$

where, β is the conversion rate of the heat work, taken as 0.9, ρ is the material density and C_p is the constant pressure specific heat capacity.

The derivation of the Johnson-Cook temperature coefficient m is as follows:

The quasi-static deformation can be considered an isothermal process. The strain rate hardening and thermal softening terms of the Johnson-Cook equation are equal to 1, and Equation (3) can be reduced.

$$\sigma = A + B\varepsilon^{n'} \quad (7)$$

Based on the quasi-static stress-strain curve, the parameters A , B and n' can be determined.

Substituting the fitted parameters into Equation (4), when the plastic strain $\varepsilon = 0$, the stress-strain relationship of the material at room temperature can be obtained as

$$\sigma = A(1 + C \ln \dot{\varepsilon}^*) \quad (8)$$

The σ - $\ln \dot{\varepsilon}^*$ curve can then be obtained using the yield stress-strain rate relationship of the material, and the parameter C value can be obtained by fitting. In this way, the Johnson-Cook model without consideration of the influence of the adiabatic temperature rise is obtained. Furthermore, it is easy to calculate the calculated value of the stress σ' corresponding to different strain rates under adiabatic temperature rise. Based on Equation (8), the ratio of the actual value of the yield stress to the calculated value of the yield stress is:

$$\frac{\sigma}{\sigma'} = 1 - (\Delta T / (T_m - T_r))^m \quad (9)$$

The calculation formula of m is then obtained as:

$$m = \frac{\ln(1 - \sigma/\sigma')}{\ln(\Delta T / (T_m - T_r))} \quad (10)$$

According to the mechanical properties of the three RMs shown in Table 2, the corresponding modified Johnson-Cook constitutive equation parameters can be fitted. The results are listed in Table 3:

Table 3. Johnson-Cook constitutive equation fitting parameters of the three Al/Ni-based RMs.

Materials	A (MPa)	B (MPa)	n'	C	m
AN	202.00	50.66	0.24	0.03	0.37
ANC	200.05	44.79	0.33	0.03	0.39
ANM	190.00	55.47	0.06	0.04	0.31

From the fitting results, it can be seen that the strain hardening index (n') of ANC under the quasi-static state is the largest, followed by that of AN, which is greater than that of ANM. The yield strengths (A) of AN, ANC, and ANM decrease successively, indicating a decrease trend due to the metal oxides added. The type of the metal oxide added determined the strengthening effect. For the characterization parameters of the thermal softening effect (m), ANC had the largest one, followed by AN and then ANM. According to the fitting result of parameter C , the difference of the strain rate effect of the three materials is not very obvious in the plastic deformation stage under dynamic loading.

4. Direct Ballistic Experiment and Calculation for SICR

4.1. Experimental Setup and Method of Calculation

The direct ballistic experiment was feasible for testing the energy release behavior of the RMs. The apparatus body was a sealed cylindrical test chamber with one end being a thin metal plate and a hard impact anvil fixed inside. After the bullet made of RMs penetrated the thin metal target plate at a certain velocity, the test chamber was heated due to the chemical reaction, in order to generate a pressure

increase. The energy release behavior was studied by measuring the quasi-static pressure inside the test chamber. The estimation formula for the impact release energy of the RMs is as follows [13]:

$$\Delta Q = \Delta p \frac{V}{\gamma - 1} \quad (11)$$

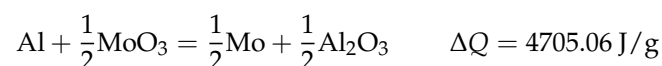
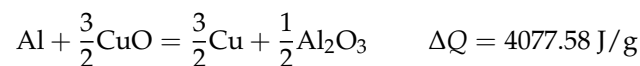
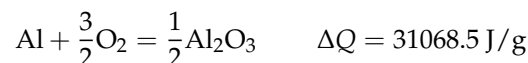
where ΔQ is the internal energy increment of the gas in the test chamber; Δp is the quasi-static pressure peak of the gas in the test chamber; V is the volume of the test chamber; γ is the ratio of the specific heat of the gas in the test chamber which is taken as 1.4 for air.

Furthermore, by subtracting the kinetic energy input from the energy in the test chamber, the extent of chemical reaction (y) of the RMs under the impact can be calculated [13]:

$$y = \frac{\Delta Q - E_k}{Q_J} \quad (12)$$

where E_k is the kinetic energy, Q_J is the chemical energy released by the complete reaction, which can be directly calculated by the heat of the chemical reactions.

The complete reaction product of Al/Ni RM (the mole ratio of Al to Ni is 1:1.46) is considered AlNi and NiO in Xiong's work [22]. Since the impact release energy of the Al/Ni-based RM was large, the following assumptions are made in the present work: (1) the Al and Ni in AN completely participate in the oxidation reaction, and (2) the metal oxides in ANC and ANM completely participate in the aluminothermic reaction with Al, and the remaining Al and Ni participate in the oxidation reaction. These chemical reaction equations are:



According to the heat released by the oxidation reaction of Al and Ni, and the aluminothermic reaction of CuO and MoO₃ [36], and with consideration of the assumptions above, the heat of the complete reactions of the three Al/Ni-based RMs can be calculated. The results are shown in Table 4.

Table 4. Complete reaction heat of the three Al/Ni -based RMs.

Materials	Q_J (kJ/g)
AN	16.16
ANC	15.44
ANM	15.57

In this work, the bullet ($\Phi 10 \text{ mm} \times 10 \text{ mm}$) was fired by a 14.5 mm ballistic gun. Its launching velocity (v) was controlled by changing the mass and the type of propellant powder, and the launching velocity was measured by two copper target coils with 2 m spacing and the time interval for breaking the copper wires (Δt). The test chamber was made of #45 steel. This chamber is a cylindrical chamber with an outer diameter of 300 mm, a length of 380 mm, a wall thickness of 3 mm and an internal capacity (V) of 27 L. The cylindrical impact anvil welded to the bottom of the test chamber, with the size of $\Phi 45 \text{ mm} \times 20 \text{ mm}$, was also made of #45 steel. A 0.5 mm thin steel target plate, which should be replaced after each experiment, was fixed by bolts on the incident surface of the test chamber. The pressure in the test chamber was measured with an air pressure sensor (measuring range: 0–1.0 MPa,

accuracy: 1%). Twenty-nine effective experiments were carried out in this work. The experimental equipment is shown in Figure 7.



Figure 7. Experimental site layout and bullet structure.

The impact release process of the RMs is complicated. The reaction threshold conditions are affected by various factors such as the microstructure and the composition. However, scholars believe that the shock temperature is the key to control the SICR. It is thus assumed that the SICR of the RMs depends on the shock temperature rise, i.e., the material is only sensitive to the heat. The chemical reaction efficiency of the RMs under the impact can be analyzed by the theoretical calculation model proposed by Zhang et al. [24,25], and the process is mainly divided into four steps:

(1) The equation of state for the mixture is calculated by that of single metal. For the RMs with strong energy release behaviors prepared by mixing single metals, it is dangerous and difficult to measure the Hugoniot data using compressive gas gun technology. Therefore, the cold energy mixture theory [24,37] and the Wu-Jing method [38,39] were adopted to calculate the Hugoniot parameters of the porous mixture (c_0 and s). The calculation parameters [37,40] of Al and Ni are listed in Table 5.

Table 5. Calculation parameters of the EOS for Al/Ni-based RMs [38,41].

Materials	ρ_0 ($\text{g}\cdot\text{cm}^{-3}$)	c_0 ($\text{km}\cdot\text{s}^{-1}$)	s	$\alpha_v \times 10^{-3}$ (K^{-1})	γ_{0K}	Y (GPa)	θ_D (K)	M ($\text{g}\cdot\text{mol}^{-1}$)
Al	2.784	5.370	1.290	6.93	2.18	0.276	423	27.0
Ni	8.875	4.590	1.440	3.81	2.00	0.380	427	58.7

Figure 8 shows the P - V curves of the Al/Ni-based RMs (Al/Ni = 2/1) with the TMD% of 97%, 75%, 55% and 35% obtained by the Wu-Jing method based on the results of the equation of state for the solid material calculated by the cold energy superposition method. It can be seen that at the same compressive specific volume V , and the lower the TMD%, the greater the pressure P , and the wider the low-pressure platform section. This means that the material with the lower TMD% could be compacted. In addition, as the mass fraction m' increasing, the difference in the P - V curve corresponding to the different mass fractions become smaller. Based on the above calculation results, the Al/Ni-based RMs (Al/Ni = 2/1) calculated using the cold energy superposition method and the Wu-Jing method can be fitted in the porous state (TMD% = 97%). The relevant Hugoniot parameters are: $c_0 = 4.417$ km/s, and $s = 1.463$.

Since the content of CuO and MoO₃ in ANC and ANM is extremely low and the Hugoniot parameters of CuO and MoO₃ has not been reported, the mass fractions of the three RMs are not obviously different. Therefore, only the Hugoniot parameters of the RMs with Al/Ni = 2/1 (AN)

were calculated, and the parameters of ANC and ANM are similar. The parameters are used for the following calculation of the impact energy release behavior of the RMs and simulation discussed in Section 5.

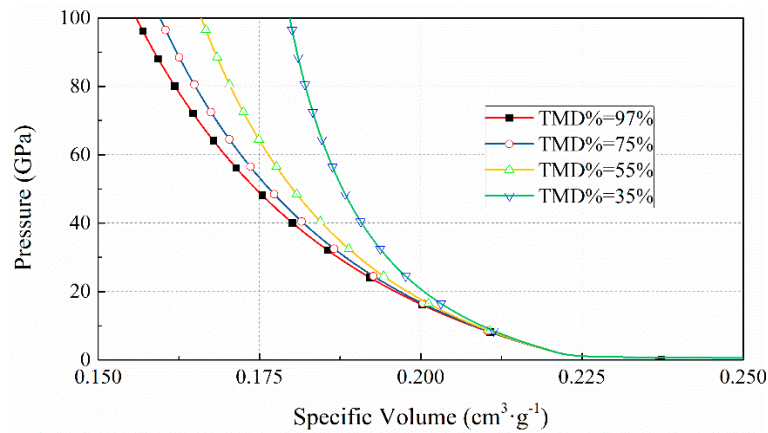


Figure 8. P-V curves of Ai/Ni-based RMs with TMD% of 97%, 75%, 55% and 35%.

(2) The impact pressure and the shock temperature of the RMs are calculated based on the one-dimensional impact wave theory and the equation of the material state. The RMs impacted the fixed target plate at an impact velocity (v). The impact wave velocities generated by the RMs and the target foil are u_{s1} and u_{s2} , respectively. The particle velocities of the RMs and the target foil compressive zone after collision are u_{a1} and u_{a2} , respectively. According to the one-dimensional impact wave theory, the initial impact wave pressure P_H of the RMs is obtained as follows [25]:

$$P_H = \rho_{01}(c_1 u_{a1} + s_1 u_{a1}^2) \tag{13}$$

where $u_{a1} = v - [-(\rho_{02}c_2 + \rho_{01}c_1 + 2\rho_{01}s_1v) + \Delta^{1/2}]/[2(\rho_{02}s_2 - \rho_{01}s_1)]$, $\Delta = (\rho_{02}c_2 + \rho_{01}c_1 + 2\rho_{01}s_1)^2 - 4(-\rho_{01})(\rho_{02}s_2 - \rho_{01}s_1)(c_1v + s_1v^2)$, and ρ_{01} and ρ_{02} are the initial densities of the RMs and the target foil, respectively. c_1, s_1 and c_2, s_2 are the linear Hugoniot parameters of the RMs and the target foil, respectively. The shock temperature T_H can be obtained from the impact wave pressure P_H [38]:

$$T_H = T_0 \exp\left(\gamma_0 \times \left(1 - \frac{V}{V_0}\right)\right) + \left(\frac{c_0^2}{C_v}\right) \exp\left(\gamma_0 \times \left(1 - \frac{V}{V_0}\right)\right) \int_0^{(1-\frac{V}{V_0})} \frac{sx^2}{(1-sx)^3} \exp(-\gamma_0 x) dx \tag{14}$$

where V_0 and T_0 are the initial specific volume and the initial temperature of the RMs; $\gamma/V = \gamma_0/V_0$, γ_0 is the initial Gruneisen coefficient of the RMs; and C_v is the constant volume specific heat of the RMs, which is a constant.

(3) The extent of the chemical reaction y is calculated with the shock temperature T_H . Considering the Arrhenius chemical kinetic equation, the Avrami-Erofeev reaction model [41–43] is used to describe the n -dimensional core/growth control method for a high-rate temperature-rise solid-state reaction. It is assumed that the reaction rate is positively correlated with the time. According to $dy/dt = C't$ (C' is a constant), the relationship between the absolute temperature T and the reactivity y and its first-order differential form can be obtained as follows [44]:

$$\frac{y^{1/2}}{n(1-y)[- \ln(1-y)]^{(1-1/n)}} = \frac{A_0}{(2C)^{1/2}} \exp\left(-\frac{E_a}{R_u T}\right) \tag{15}$$

$$\frac{dT}{dy} = \frac{R_u T^2}{E_a} \left[\frac{1}{2y} - \frac{n \ln(1-y) + n - 1}{n(1-y)[- \ln(1-y)]} \right] \tag{16}$$

where, R_u is the universal gas constant, E_a is the apparent activation energy, and n is the reaction mechanism parameter. The extent of the chemical reaction y can be calculated from the shock temperature T_H using Formula (16) by considering the reaction threshold (T_{cr}, y_{cr}).

(4) The pressure P' and the temperature T' are updated after the chemical reaction [22]:

$$P' = \frac{-yQ_J + P_H\left(\frac{V_0-V}{2} - \frac{V}{\gamma}\right)}{\frac{V_0-V}{2} - \frac{V}{\gamma}} \quad (17)$$

$$T' = T_0 \exp\left[-\int_{V_0}^V \left(\frac{\gamma}{V}\right)dV\right] + \frac{V_0}{\gamma_0 C_V}(P - P_S) \quad (18)$$

where P_s is the isentropic pressure, which is a function of the specific volume V , and its form is determined.

4.2. Results

As typical overpressure signals, the results of #1 experiment are shown in Figure 9. The quasi-static pressure in the test chamber was obtained using the original pressure signal low-pass filtered by a cutoff frequency of 400 Hz. The signal can be divided into two stages: The first stage is pressurization, i.e., the pressure increases until reaching a peak mainly due to air in the test chamber rapidly expanding, which is caused by the chemical reaction of the RMs under the impact, and the time range is 0–5 ms; The second stage is the pressure release, i.e., the pressure in the test chamber is slowly reduced due to the chemical reaction finishing, the poor airtightness of the test chamber and the heat conduction effect, and the time range is 65–75 ms.

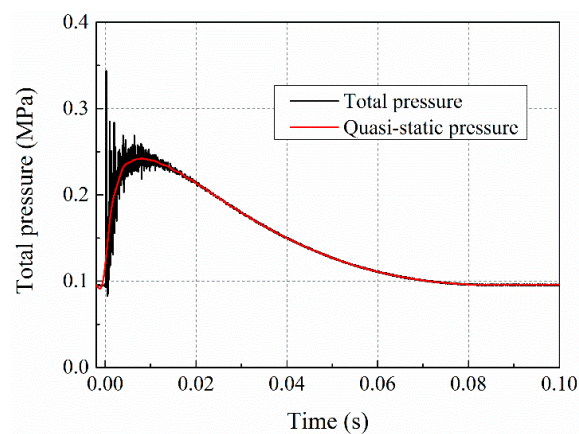


Figure 9. Typical overpressure results (for #1 experiment in Table 6).

According to Formulas (10)–(13) and 27 effective experimental results, the impact velocity v , the quasi-static pressure peak Δp , the release energy ΔQ , the impact pressure P_H , the shock temperature T_H and the extent of the chemical reaction y for the materials are listed or calculated in Table 6.

Figure 10 shows the velocity-release energy relationships of the three RMs, and the relationships among them are linearly fitted. The impact velocity thresholds of the impact release energy for the three materials are 1000–1100 m/s. At the same impact velocity, the greater the release energy of material, the greater the slope of the fitted curve of velocity-release energy. According to the fitting results ($k_{AN} = 7.509$ J·s/m, $k_{ANC} = 9.748$ J·s/m and $k_{ANM} = 15.384$ J·s/m), the release energy of the three RMs from large to small is that: ANM > ANC > AN, i.e., the release energy of the materials with the metal oxide added is greater at the same impact velocity. For the different release energies attribute to the different chemical reaction types under the impact: CuO and MoO₃ can react with Al for the aluminothermic reaction, in which the reaction rate and the heat of MoO₃ are greater than those of

CuO [37]. Therefore, the release energy of ANM is greater than that of ANC. The release energy of both ANM and ANC is greater than that of AN due to the added metal oxide.

Table 6. Experimental and computational results of the direct ballistic experiment.

No.	Materials	Mass (g)	Impact Velocity v (m/s)	Quasi-Static Pressure Peak Δp (MPa)	Release Energy ΔQ^1 (J)	P_H (GPa)	T_H (K)	y
#1	AN	3.29	1730	0.1461	4938.43	21.61	473.02	0.0929
#2	AN	3.26	1785	0.1653	5964.20	21.66	473.67	0.1132
#3	AN	3.27	1445	0.0834	2215.58	20.93	464.40	0.0419
#4	AN	3.28	1437	0.0697	1318.20	20.90	464.02	0.0249
#5	AN	3.25	1250	0.0536	1078.94	20.00	452.99	0.0205
#6	AN	3.28	1191	0.0432	589.69	19.63	448.62	0.0111
#7	AN	3.29	1097	0.0351	389.64	18.96	440.79	0.0073
#8	AN	3.25	1516	0.1088	3609.33	21.17	467.41	0.0687
#9	AN	3.27	1532	0.0960	2642.62	21.21	468.01	0.0500
#10	AN	3.27	1866	0.1604	5134.00	21.69	474.07	0.0971
#11	ANM	3.24	1805	0.2800	13,622.00	21.61	475.48	0.2700
#12	ANM	3.24	1809	0.2583	12,133.83	21.62	475.54	0.2405
#13	ANM	3.24	1637	0.2083	9719.02	21.33	471.82	0.1927
#14	ANM	3.22	1591	0.2141	10,376.39	21.22	470.32	0.2070
#15	ANM	3.22	1474	0.1302	5289.82	20.83	465.46	0.1055
#16	ANM	3.23	1430	0.1657	7882.24	20.66	463.24	0.1567
#17	ANM	3.24	1216	0.0718	2451.08	19.52	449.30	0.0486
#18	ANM	3.26	1274	0.1364	6,561.39	19.88	453.60	0.1293
#19	ANM	3.26	1009	0.0334	595.03	17.92	430.85	0.0117
#20	ANM	3.23	1005	0.0286	299.31	17.89	430.45	0.0060
#21	ANC	3.29	1788	0.1979	8099.28	21.67	473.28	0.1594
#22	ANC	3.28	1830	0.1907	7380.05	21.69	473.49	0.1457
#23	ANC	3.29	1592	0.1463	5706.06	21.40	469.86	0.1123
#24	ANC	3.28	1632	0.1388	5000.98	21.48	470.90	0.0988
#25	ANC	3.3	1431	0.1446	6381.69	20.92	463.8	0.1253
#26	ANC	3.29	1212	0.0496	931.59	19.83	450.49	0.0183
#27	ANC	3.29	1177	0.0674	2270.63	19.60	447.81	0.0447
#28	ANC	3.28	1889	0.2248	9321.95	21.69	473.48	0.1841
#29	ANC	3.27	1322	0.0856	2920.54	20.44	457.92	0.0579

¹ The kinetic energy of specimens has been subtracted from the release energy (J).

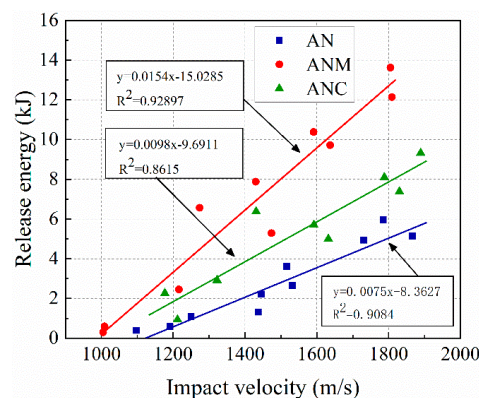


Figure 10. Release energy distribution of three Al/Ni-based RMs.

According to the above calculation results and Formula (13), the chemical reaction parameters E_a , the reaction mechanism parameter n and the reaction thresholds (T_{cr} , y_{cr}) of the three materials were obtained using least squares fitting. The calculated data points and the fitting curves are shown in Figure 11. The parameters obtained by fitting are shown in Table 7.

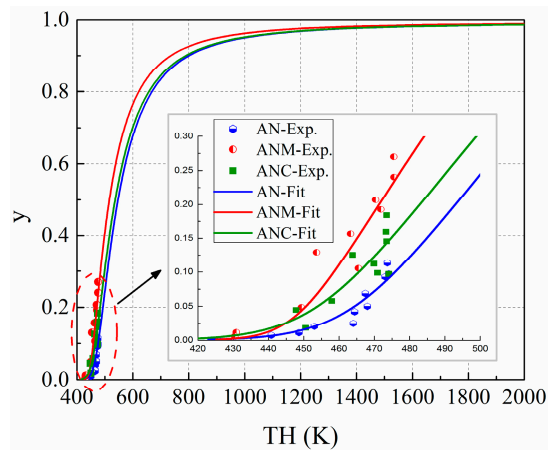


Figure 11. T_H - y fitting results of three RMs.

Table 7. T_H - y fitting results of the three RMs.

Materials	y_{cr}	T_{cr} (K)	E_a (kJ/mol)	n
AN	0.001	422	20.88	1.60
ANC	0.001	411	20.45	1.65
ANM	0.001	425	20.00	1.77

From the T_H - y fitting curves, it can be observed that the chemical reaction mechanism parameter n of the three materials from large to small is as follows: ANM > ANC > AN. AN has the largest apparent activation energy (E_a), ANC has the second largest, and that of ANM is the smallest. The parameter n affects the formation and growth rate of the product nucleus in the n -dimensional nucleus/growth controls of the Avrami-Erofeev reaction model, and the parameter E_a characterizes the energy requirement for the reactive molecules to impact effectively. The greater the E_a value, the easier and faster the chemical reaction can be. Therefore, both E_a and n determine the extent of chemical reaction. Due to the thermal reaction of the metal oxides CuO, MoO₃ and Al, the reaction rate of ANM and ANC is greater, and the reaction rate of the MoO₃ aluminothermic reaction is greater than that of the CuO aluminothermic reaction. Therefore, the chemical reaction mechanism parameters n of ANM is the greatest and the apparent activation energy E_a is the smallest.

5. The Simulation of the Impact Energy Release Process

5.1. The User's Subroutines Defining Material Model

The impact energy release behavior of the RMs was simulated with the user-defined material models of LS-DYNA software, adding the equation of state describing the normal stress-strain relationship of the material and a chemical kinetic equation describing the relationship between the temperature and the extent of chemical reaction. The behavior was also on the deviatoric stress-strain relationship represented by the Johnson-Cook constitutive model. The calculation program structure is shown in Figure 12.

The mechanical-thermo-chemical coupled user-defined constitutive model program differs from the conventional constitutive model program that comes with the LS-DYNA software (version 971 smp d R7.0.0, Livermore Software Technology Corp., Livermore, CA, U.S.) in the following three points: (1) the program uses the Gruneisen equation of state to calculate the hydrostatic pressure P from the bulk strain v , (while the conventional constitutive model uses a fixed bulk modulus K to define the P - V relationship); (2) the chemical kinetic equation is added, which can describe the relationship between the unit temperature T and the extent of chemical reaction y ; and (3) the unit failure model is eliminated,

because it is impossible to calculate the internal extent of the chemical reaction due to the element failure being set to the element directly-delete in the calculation process of the LS-DYNA software.

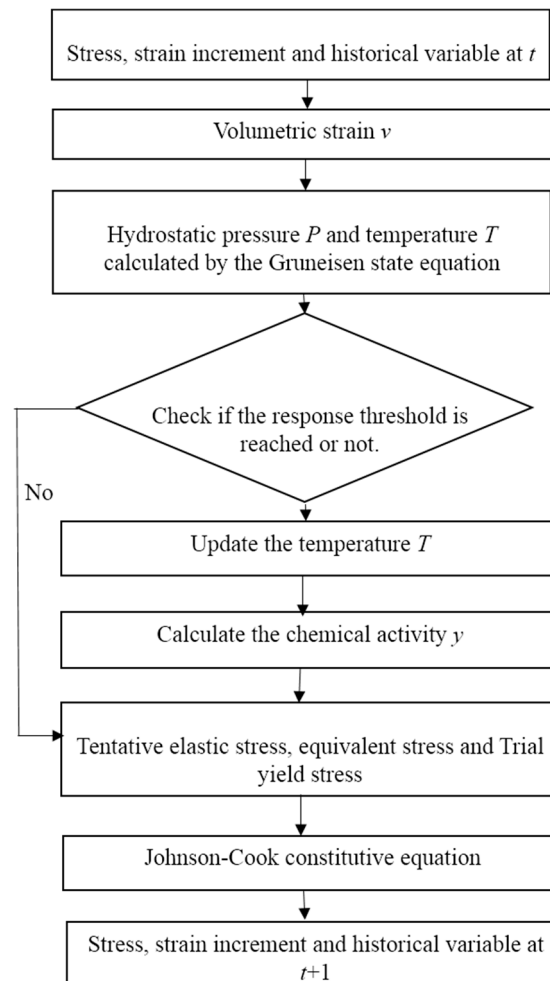


Figure 12. Mechanical-thermo-chemical coupled user-defined constitutive model program structure in LS-DYNA software.

5.2. Finite Element Model

The finite element model is shown in Figure 13, which is a three-dimensional model of symmetry about the XY plane. The red PART is a bullet (Semi-cylindrical with size of $\Phi 10 \text{ mm} \times 10 \text{ mm}$), the blue PART is the target plate (Semi-cylindrical with size of $\Phi 45 \text{ mm} \times 20 \text{ mm}$). Considering the far-end from the bullet of the target plate as a rigid boundary, the degree of freedom of all nodes at the uppermost end is constrained. The translational and rotational degrees of freedom of the Z-directions of all nodes on the $Z = 0$ plane are constrained. All of the mesh grids of the model are hexahedral. There are 1–440 elements for the bullet and 441–19,140 elements for the target plate.

In the simulation, the materials under working conditions with impact velocities of 1000 m/s, 1300 m/s, 1500 m/s and 1700 m/s were simulated by the ALE algorithm. The bullet material was simulated by the user-defined material models in LS-DYNA software. The Johnson-Cook constitutive parameter was taken from Table 3, and the parameters of the Gruneisen equation of state were taken from the fitting result in Figure 6 (as mentioned in Section 4.2). The parameters of the chemical kinetic equation were taken from Table 7; the target material is #45 steel, which is described by LS-DYNA's original *MAT_JOHNSON_COOK [45] (p.70.MAT) constitutive model and *EOS_GRUNEISEN [45] (p.15.12) equation of state. The material parameters are taken from Tables 8–11.

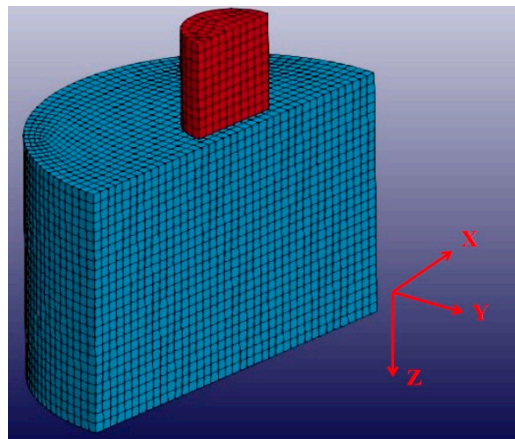


Figure 13. Numerical simulation model of impact energy release behavior.

Table 8. Parameters of the constitutive model [46].

Materials	Density ρ g/cm ³	Bulk Modulus K (GPa)	Shear Modulus G (GPa)	A (MPa)	B (MPa)
#45 steel	7.890	157.8	77	792	298
Tr (K)	Tm (K)	$EPSO$ (s ⁻¹)	n'	m	
298	1793	0.01	0.26	1.03	

Johnson-Cook constitutive model: $\sigma_y = (A + B\epsilon_{eff}^p)^n (1 + C \ln \dot{\epsilon}^*) (1 - T^{*m})$

Table 9. Parameters of the failure model [46].

Materials	D_1	D_2	D_3	D_4	D_5
#45 steel	0.8	0	0	0	0

Failure model: $\epsilon_f^p = (D_1 + D_2 e^{D_3 \sigma^*}) (1 + D_4 \ln \dot{\epsilon}^*) (1 + D_5 T^{*m})$

Table 10. Parameters of equation of state [46].

Materials	Volumetric Sound Velocity c (km/s)	S_1	S_2	S_3	a	Initial Internal Energy E_0
#45 steel	5.13	1.86	0	0	2.77	0

Gruneisen EOS: $p = \frac{\rho_0 c^2 \mu [1 + (1 - \frac{\gamma_0}{2}) \mu - \frac{\mu^2}{2}]}{[1 - (S_1 - 1)\mu - S_2 \frac{\mu^2}{\mu + 1} - S_3 \frac{\mu^3}{(\mu + 1)^2}]^2} + (\gamma_0 + a\mu)E$

Table 11. Parameters of the thermal constitutive model [46].

Materials	Constant Volume Heat (J·kg ⁻¹ ·K ⁻¹)	Thermal Conductivity (W·m ⁻¹ ·K ⁻¹)
#45 steel	460	48

5.3. Simulation Analysis for Impact Energy Release Behavior

Figure 14 shows the extent of the chemical reaction y nephogram of each impact velocity at the maximum deformation of the Ai/Ni-based RMs. It can be observed that the higher the impact velocity of the bullet, the greater the extent of the chemical reaction of the material.

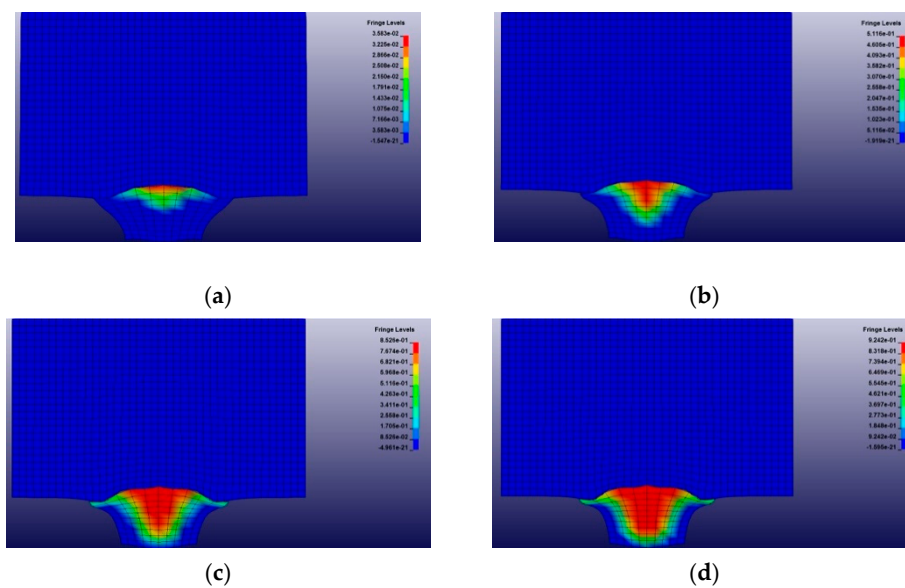


Figure 14. Extent of the chemical reaction γ nephogram at different impact velocities under maximum deformation of the Ai/Ni-based RMs: (a) 1000 m/s; (b) 1300 m/s; (c) 1500 m/s; (d) 1700 m/s.

For the Ai/Ni-based RMs with an impact velocity of 1300 m/s, the time-history curve information of the historical variables of the A42, B34 and C96 units on the bullet were extracted, i.e., the time-history curve of the extent of chemical reaction γ in a unit. As shown in Figure 15a, the γ differs due to the different loads of each unit. It can be seen from Figure 15b that the γ rising to the maximum value from zero, which can be considered the end of chemical reaction, and which takes a few microseconds for each unit. This is in the same magnitude of the time width of the impact wave front, and it is consistent with the assumption of the shock-induced chemical reaction theory.

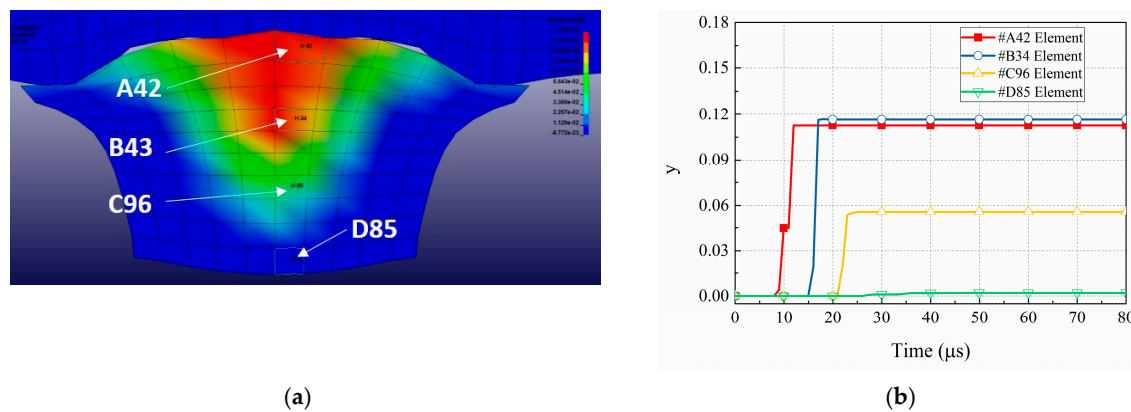


Figure 15. Time-history curve of the extent of the chemical reaction for three units of the Ai/Ni-based RMs at an impact velocity of 1300 m/s: (a) location of elements; (b) time-history curves of the extent of the chemical reaction γ .

The time-history curve information of the extent of the chemical reaction γ for all of the units in each working condition was extracted. According to the volume of each unit, the overall mass average extent of the chemical reaction of the bullet was calculated and compared with the experimental results in Section 4. As shown in Figure 16 and Table 12, the relationship between the impact velocity v and the extent of the chemical reaction γ is considered linear. It can be observed that the error of slope a is 20–30%, and the error of the intercept b is 30–40%.

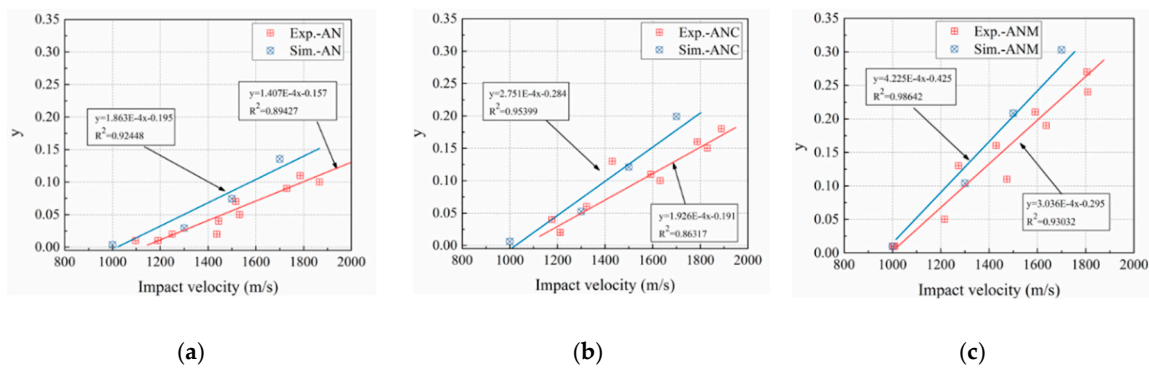


Figure 16. Comparison of the direct ballistic experiment results and the simulation fitting results: (a) AN; (b) ANC; (c) ANM.

Table 12. Comparisons of the experimental results with the simulation results.

Materials	Fitting Parameters	Experiment Values	Simulation Values	Relative Errors
AN	Slope a (s/m)	1.41×10^{-4}	1.86×10^{-4}	24.49%
	Intercept b	-0.157	-0.195	19.72%
ANC	Slope a (s/m)	1.93×10^{-4}	2.75×10^{-4}	29.98%
	Intercept b	-0.191	-0.284	32.52%
ANM	Slope a (s/m)	3.04×10^{-4}	4.23×10^{-4}	28.14%
	Intercept b	-0.295	-0.425	30.62%

The main reasons for those errors are as follows: (1) in the direct ballistic experiment, a chemical reaction with different extent occurred when the bullet strikes the thin-walled target plate, resulting in a loss of reactants. With the bullet velocity increasing, the mass loss of the reactants outside the test chamber increased. This leads to differences in the mass and the calculated release energy between in the simulation and in the experiment increases, resulting in the simulation slope being generally larger than the experimental slope. (2) The heat conduction effect was ignored in the process of numerical simulation. However, this effect exists in the experiment, including different degrees of heat conduction on the wall of the test chamber. The pressure loss also occurs through the perforation of the thin-walled target plate in the test chamber, which increases with the increase of the pressure difference between inside and the outside of the test chamber. The Johnson-Cook constitutive model considering the mechanical-thermo-chemical coupling effect cannot be solved jointly with the original thermal constitutive model of the LS-DYNA software to simulate the heat conduction effect among the bullet, target plate and air.

In summary, although the error between the simulation and experimental results exists (the error of slope a is 20–30%, and the error of intercept b is 30–40%), those errors are regarded as reasonable. Therefore, it can be concluded that the self-developed Johnson-Cook constitutive model considering the mechanical-thermo-chemical coupling effect could produce a numerical simulation for the impact energy release behavior of the Al/Ni-based RMs.

6. Conclusions

In this work, the three Al/Ni-based RMs (AN, ANC and ANM) prepared with the hot-pressing forming process were used as the research objects, and the mechanical properties and the impact energy release behavior were studied. Based on the experimental data, the theoretical calculation for the impact energy release behavior and the development of the LS-DYNA user defined material model considering the mechanical-thermo-chemical coupling effect, i.e., the integrated numerical simulation of the mechanical behavior and the chemical reaction release behavior, was accomplished. The main conclusions are as follows:

- (1) The compressive stress-strain curves of the three Al/Ni-based RMs can be described by the Johnson-Cook constitutive model. The compressive strength is 200MPa–300 MPa and there is a certain strain rate effect. The addition of the metal oxide can impair the mechanical properties of the Al/Ni-based RMs, and the degree depending on the type of metal oxide. According to the SEM observation, the RMs prepared by the hot-pressing forming process can be approximated seen as porous materials with a high TMD%.
- (2) The impact energy release behavior of the Al/Ni-based RMs at different impact velocities was studied with a direct ballistic experiment. According to the impact velocity-release energy relationship, the impact energy release behavior of the three Al/Ni-based RMs can be arranged as: ANM > ANC > AN, that is, the impact release property of the material containing metal oxide is better at the same impact velocity. Both CuO and MoO₃ can react with Al for the aluminothermic reaction, and the thermal reaction rate and the heat of reaction of MoO₃ are greater than that of CuO. Therefore, the chemical reaction mechanism parameter n and the apparent activation energy E_a of the three Al/Ni-based RMs are different. The arrangement of the extent of the chemical reaction (i.e., the rates of chemical reaction) of the three materials from large to small is: ANM > ANC > AN. It can be considered that the metal oxide can improve the energy release behavior of the Al/Ni-based RMs. AN without metal oxide added has the maximal complete heat of reaction, while ANM with metal oxide added has the best energy release behavior.
- (3) Based on the thermochemical model of shock-induced chemical reaction considering the efficiency of the chemical reaction, a Johnson-Cook constitutive model considering the mechanical-thermo-chemical coupling effect was developed. The impact energy release behavior of the Al/Ni-based RMs was simulated in LS-DYNA software, and the numerical simulation results were verified by the experimental results. It was found that the slope a of the numerical simulation was 20–30% larger than that in the experiment. The constitutive model developed in this work can achieve an integrated numerical simulation for the impact energy release behavior of the Al/Ni-based RMs.

Author Contributions: Conceptualization, K.R., R.C. and S.L.; Data curation, K.R. and R.C.; Formal analysis, K.R.; Investigation, K.R.; Methodology, K.R., R.C., Y.L. and S.L.; Resources, R.C., Y.L., S.L., X.Z. and J.D.; Software, K.R.; Supervision, R.C., Y.L. and S.L.; Validation, K.R., R.C., Y.L., S.L., X.Z. and J.D.; Writing – original draft, K.R.; Writing – review & editing, R.C., Y.L., S.L., X.Z. and J.D.

Funding: This research was funded by the National Natural Science Foundation of China (No. 11672328).

Conflicts of Interest: The authors declare no conflict of interest.

References

1. National Research Council. *Advanced Energetic Materials*; National Academies Press: Washington, DC, USA, 2004; pp. 20–23, ISBN 978-0-309-16647-8. [[CrossRef](#)]
2. Zhang, X.F.; Zhao, X.N. Review on multifunction reactive metals. *Chin. J. Energ. Mater.* **2009**, *17*, 731–739. [[CrossRef](#)]
3. Ferranti, L., Jr.; Thadhani, N.N. Dynamic Mechanical Behavior Characterization of Epoxy-Cast Al + Fe₂O₃ Thermite Mixture Composites. *Metall. Mater. Trans. A* **2007**, *38*, 2697–2715. [[CrossRef](#)]
4. Ren, H.; Liu, X.; Ning, J. Microstructure and mechanical properties of W-Zr reactive materials. *Mater. Sci. Eng. A* **2016**, *660*, 205–212. [[CrossRef](#)]
5. Eakins, D.E.; Thadhani, N.N. The shock-densification behavior of three distinct Ni + Al powder mixtures. *Appl. Phys. Lett.* **2008**, *92*, 111903. [[CrossRef](#)]
6. Thadhani, N.N. Shock-induced chemical reactions and synthesis of materials. *Prog. Mater. Sci.* **1993**, *37*, 117–226. [[CrossRef](#)]
7. Thadhani, N.N.; Graham, R.A.; Royal, T.; Dunbar, E.; Anderson, M.U.; Holman, G.T. Shock-induced chemical reactions in titanium–silicon powder mixtures of different morphologies: Time-resolved pressure measurements and materials analysis. *J. Appl. Phys.* **1997**, *82*, 1113–1128. [[CrossRef](#)]

8. Zhao, P.D.; Lu, F.Y.; Li, J.L.; Chen, R.; Xu, S.L.; Yang, S.Q. The dynamic compressive properties of PTFE/Al reactive materials. *Chin. J. Energ. Mater.* **2009**, *17*, 459–462. [[CrossRef](#)]
9. McGregor, N.; Sutherland, G. Plate impact experiments on a porous Teflon-Aluminum mixture. In Proceedings of the AIP Conference Proceedings 2004, Sacramento, CA, USA, 4–5 August 2004; Volume 706, pp. 1001–1004. [[CrossRef](#)]
10. Mock, W., Jr.; Holt, W.H. Impact Initiation of Rods of Pressed Polytetrafluoroethylene (PTFE) and Aluminum Powders. In Proceedings of the AIP Conference Proceedings 2006, Jammu, India, 17–18 April 2006; Volume 845, pp. 1097–1100. [[CrossRef](#)]
11. Herbold, E.B.; Nesterenko, V.F.; Benson, D.J.; Cai, J.; Vecchio, K.S.; Jiang, F.; Addiss, J.W.; Walley, S.M.; Proud, W.G. Particle size effect on strength, failure, and shock behavior in polytetrafluoroethylene-Al-W granular composite materials. *J. Appl. Phys.* **2008**, *104*, 103903. [[CrossRef](#)]
12. Raftenberg, M.N.; Mock, W., Jr.; Kirby, G.C. Modeling the impact deformation of rods of a pressed PTFE/Al composite mixture. *Int. J. Impact Eng.* **2008**, *35*, 1735–1744. [[CrossRef](#)]
13. Ames, R.G. Vented Chamber Calorimetry for Impact-Initiated Energetic Materials. In Proceedings of the 43rd AIAA Aerospace Sciences Meeting and Exhibit, Reno, NV, USA, 10–13 January 2005. [[CrossRef](#)]
14. Ames, R.G. *Energy Release Characteristics of Impact-Initiated Energetic Materials*; Materials Research Society: Triangle Park, NC, USA, 2006. [[CrossRef](#)]
15. Yang, Y.; Gould, R.D.; Horie, Y.; Iyer, K.R. Shock-induced chemical reactions in a Ni/Al powder mixture. *Appl. Phys. Lett.* **1997**, *70*, 3365–3367. [[CrossRef](#)]
16. Eakins, D.E.; Thadhani, N.N. Investigation of Shock-Induced Reactions in a Ni + Al Powder Mixture. In Proceedings of the 14th APS Topical Conference on Shock Compression of Condensed Matter, Baltimore, MD, USA, 31 July–5 August 2005.
17. Mason, B.A.; Groven, L.J.; Son, S.F. The role of microstructure refinement on the impact ignition and combustion behavior of mechanically activated Ni/Al reactive composites. *J. Appl. Phys.* **2013**, *114*, 113501. [[CrossRef](#)]
18. Wang, H.F.; Liu, Z.W.; Yu, W.M.; Wang, H. Experimental Investigation of Energy Release Characteristics of Reactive Fragments. *Trans. Beijing Inst. Technol.* **2009**, *8*, 663–666. [[CrossRef](#)]
19. Zhang, X.F.; Shi, A.S.; Qiao, L.; Zhang, J.; Zhang, Y.G.; Guan, Z.W. Experimental study on impact-initiated characters of multifunctional reactive metals. *J. Appl. Phys.* **2013**, *113*, 083508. [[CrossRef](#)]
20. Luo, P.; Wang, Z.; Jiang, C.; Liang, M.; Qiang, L. Experimental study on impact-initiated characters of W/Zr energetic fragments. *Mater. Des.* **2015**, *84*, 72–78. [[CrossRef](#)]
21. Xiong, W.; Zhang, X.; Tan, M.; Chuang, L.; Xue, W. The Energy Release Characteristics of Shock-Induced Chemical Reaction of Al/Ni Composites. *J. Phys. Chem. C* **2016**, *120*, 24551–24559. [[CrossRef](#)]
22. Ji, C.; He, Y.; Wang, C.T.; He, Y.; Pan, X.C.; Jiao, J.J.; Guo, L. Investigation on shock-induced reaction characteristics of an Al/Ni composite processed via accumulative roll-bonding. *Mater. Des.* **2017**, *116*, 591–598. [[CrossRef](#)]
23. Zhang, X.F.; Qiao, L.; Shi, A.S.; Zhang, J.; Guan, Z.W. A cold energy mixture theory for the equation of state in solid and porous metal mixtures. *J. Appl. Phys.* **2011**, *110*, 013506. [[CrossRef](#)]
24. Zhang, X.F.; Zhao, X.N.; Qiao, L. Theory analysis on shock-induced chemical reaction of reactive metal. *Explosion Shock Waves* **2010**, *30*, 145–151. [[CrossRef](#)]
25. Do, I.P.H.; Benson, D.J. Modeling shock-induced chemical reactions. *Int. J. Comput. Eng. Sci.* **2000**, *1*, 61–79. [[CrossRef](#)]
26. Do, I.P.H.; Benson, D.J. Micromechanical modeling of shock-induced chemical reactions in heterogeneous multi-material powder mixtures. *Int. J. Plast.* **2001**, *17*, 641–668. [[CrossRef](#)]
27. Reding, D.J. Shock Induced Chemical Reactions in Reactive Metals. Ph.D. Thesis, Georgia Institute of Technology, Atlanta, GA, USA, 4 December 2008.
28. Reding, D.J.; Hanagud, S. Chemical reactions in reactive powder metal mixtures during shock compression. *J. Appl. Phys.* **2009**, *105*, 175–180. [[CrossRef](#)]
29. Reding, D.J. Pore collapse in powder metal mixtures during shock compression. *J. Appl. Phys.* **2009**, *105*, 321–356. [[CrossRef](#)]
30. Austin, R.A. Modeling Shock Wave Propagation in Discrete Ni/Al Powder Mixtures. Ph.D. Thesis, Georgia Institute of Technology, Atlanta, GA, USA, 11 November.

31. Qiao, L.; Zhang, X.F.; He, Y.; Zhao, X.N.; Guan, Z.W. Multiscale modelling on the shock-induced chemical reactions of multifunctional reactive metals. *J. Appl. Phys.* **2013**, *113*, 173513–173513. [[CrossRef](#)]
32. Qiao, L. Study on the Effects of Mesoscale Characteristic on Shock Reaction Behaviour of Multifunctional Reactive Metals. Ph.D. Thesis, Nanjing University of Science and Technology, Nanjing, China, 13 June 2013.
33. Lu, F.Y.; Chen, R.; Lin, Y.L.; Zhao, P.D.; Zhang, D. *Hopkinson Bars Experimental Technique*, 1st ed.; Science Press: Beijing, China, 2013; pp. 56–57, ISBN 978-7-0303-8434-8.
34. Johnson, G.R.; Cook, W.H. A constitutive model and data for metals subjected to large strains, high strain rates and high temperatures. In Proceedings of the Seventh International Symposium on Ballistics, The Hague, The Netherlands, 19–21 April 1983; pp. 541–547.
35. Meyers, M.A.; Subhash, G.; Kad, B.K.; Prasad, L. Evolution of Microstructure and Shear-Band Formation in α -hcp Titanium. *Mech. Mater.* **1994**, *17*, 175–193. [[CrossRef](#)]
36. Fischer, S.; Grubelich, M. A survey of combustible metals, thermites, and intermetallics for pyrotechnic applications. In Proceedings of the 32nd Joint Propulsion Conference and Exhibit, Lake Buena Vista, FL, USA, 1–3 July 1996. [[CrossRef](#)]
37. Tang, W.H.; Zhang, R.Q. *Introduction to Theory and Computation of Equations of State*, 1st ed.; Higher Education Press: Beijing, China, 2008; pp. 126–128, ISBN 978-7-8102-4566-1.
38. Wu, Q.; Jing, F. Unified thermodynamic equation-of-state for porous materials in a wide pressure range. *Appl. Phys. Lett.* **1995**, *67*, 49–51. [[CrossRef](#)]
39. Wu, Q.; Jing, F. Thermodynamic equation of state and application to Hugoniot predictions for porous materials. *J. Appl. Phys.* **1996**, *80*, 4343–4349. [[CrossRef](#)]
40. Marsh, S.P. *LASL Shock Hugoniot Data*, 1st ed.; University of California Press: Berkeley, CA, USA, 1980; p. 112, ISBN 0-520-04008-2.
41. Avrami, M. Kinetics of phase change. I General theory. *J. Chem. Phys.* **1939**, *7*, 1103–1112. [[CrossRef](#)]
42. Avrami, M. Kinetics of phase change. II transformation-time relations for random distribution of nuclei. *J. Chem. Phys.* **1940**, *8*, 212–224. [[CrossRef](#)]
43. Avrami, M. Kinetics of phase change. III: granulation, phase change and microstructure. *J. Chem. Phys.* **1941**, *9*, 177–184. [[CrossRef](#)]
44. Ortega, A.; Maqueda, L.P.; Criado, J.M. The problem of discerning Avrami-Erofeev kinetic models from the new controlled rate thermal analysis with constant acceleration of the transformation. *Thermochim. Acta* **1995**, *254*, 147–152. [[CrossRef](#)]
45. LS-DYNA@Keyword User's Manual Volume 1, Livermore Software Technology Corporation (LSTC). Available online: http://ftp.lstc.com/anonymous/outgoing/jday/manuals/ls-dyna_971_manual_k_rev1.pdf (accessed on 17 August 2009).
46. Shi, T.Y.; Li, Y.C.; Zhang, S.M. *Explicit Dynamic Analysis Based on ANSYS/LS-DYNA 8.1*, 1st ed.; Tsinghua University Press: Beijing, China, 2005; pp. 68–76, ISBN 978-7-3021-0135-2.

